energy&fuels

Article

pubs.acs.org/EF

Mercury Interaction with the Fine Fraction of Coal-Combustion Fly Ash in a Simulated Coal Power Plant Flue Gas Stream

Adam D. Jew,[*,†,‡] Erik C. Rupp,[‡] Dawn L. Geatches,[‡] Ji-Eun Jung,[‡] Gabriela Farfan,[†] Louisa Bahet,[‡] James C. Hower,[§] Gordon E. Brown, Jr.,[†,∥,⊥] and Jennifer Wilcox[‡]

[†]Department of Geological Sciences, School of Earth, Energy, and Environmental Sciences, Stanford University, Stanford, California 94305-2115, United States

[‡]Department of Energy Resources Engineering, School of Earth, Energy, and Environmental Sciences, Stanford University, Stanford, California 94305-2220, United States

[§]Center for Applied Energy Research, University of Kentucky, Lexington, Kentucky 40511, United States

[∥]Department of Chemical Engineering, Stanford University, Stanford, California 94305, United States

[⊥]Department of Photon Science and Stanford Synchrotron Radiation Lightsource, SLAC National Accelerator Laboratory, Menlo Park, California 94025, United States

ABSTRACT: Mercury associated with fly ash is a significant contaminant released in flue gas emissions from coal-fired power plants. This work focuses on the association of Hg with other elements and phases as well as the molecular-level speciation of Hg in bulk and <0.1 μm sized fly ash particles reacted with a Hg-containing simulated flue gas stream. Following reaction under conditions chosen to simulate an electrostatic precipitator operating at 140 °C, fly ash (bulk and ≤0.1 μm) from a Kentucky power plant was analyzed using microscopic and spectroscopic techniques. The ≤0.1 μm fraction dominates Hg uptake, with total Hg concentrations increasing from 100 ppb to 610 ppm after reaction, whereas bulk ash concentrations increase from 11 to 164 ppb. Synchrotron-based micro-X-ray fluorescence mapping of the reacted ≤0.1 μm fraction showed that Hg is present in two major regions: Fe-rich areas and Hg hot spots not associated with Fe. X-ray absorption spectroscopic analysis revealed that Hg is associated with Br and Cl, is bound to iron oxides, and occurs as HgS (cinnabar). Fourier transform infrared (FTIR) spectroscopic analysis of the fine fraction revealed carboxylic, alcoholic, and alkane functional groups. Density functional theory simulation of the vibrational frequencies of a carboxylic group bonded to Hg reproduced the same frequency shifts and peak intensity reductions (relative to carboxylic acid alone) observed in the experimental FTIR spectrum of the Hg-reacted fly ash fine fraction, suggesting Hg(II) binding to organic matter. Our results reveal complex interactions between Hg and coal fly ash in the combustion stream that produces less bioavailable forms of Hg than Hg^0 present in the unreacted flue gas. Such information is critical for safe disposal of Hg-containing fly ash in landfills or use in cementitious products.

INTRODUCTION

Anthropogenic Hg release to the environment is a serious human and environmental concern. Emissions of Hg from coal combustion are estimated to comprise 24% of all anthropogenic Hg release and 42% of the unintentional/byproduct Hg release.[1] Motivation for research on Hg interactions with coal fly ash in coal-fired power plant flue gas streams comes from new federal standards for mercury emissions recently adopted by the United States Environmental Protection Agency (EPA). The EPA finalized its Mercury and Air Toxic Standards (MATS) for existing power plants in February 2012 and new power plants in April 2013, requiring existing coal-fired power plants to limit their Hg emissions to below 5.9−54.5 g/GWh, depending on the type of power plant and coal source.[2] New coal-fired units will be held to even stricter standards, with emission limits below 1.4 g/GWh. With the implementation of these new regulations, new strategies for effective removal of Hg from flue gas streams are necessary for the coal energy industry. In coal-fired power plant exhaust streams, Hg can be found in at least three forms: elemental (Hg^0) and oxidized (Hg^{2+}) (both in the vapor phase) and Hg bound to particulates (Hg_p). Elemental mercury is highly volatile and not readily removed from the gas stream, whereas Hg^{2+} and Hg_p can typically be removed through standard emission controls.[3−9] Because Hg release to the atmosphere is a major concern, there has been significant research on Hg uptake by three key sorbents—activated carbon, modified activated carbon, and coal fly ash.[10−21] Among these three sorbents,[22,23] coal fly ash is particularly important because the ash is a waste material already present in the flue gas stream with volatile Hg, and even with 99.95% capture efficiency, the average coal-fired power plant releases approximately 1 ton of coal fly ash to the atmosphere per day.[24]

Coal fly ash is highly heterogeneous and consists of inorganic and organic materials that are crystalline or amorphous.[14,18,20,25−29] In addition to their compositional heterogeneity, coal fly ash particles vary widely in size, ranging from 100s of μm to <50 nm in diameter.[18,25,27,28,30] Adding to this complexity is the fact that a number of toxic elements are associated with coal fly ash, including Hg, Se, As, Cr, Cu, and Ni.[4,14,16,18,20,31−36] Use of a variety of techniques is necessary to

Received: June 6, 2015
Revised: August 7, 2015
Published: August 11, 2015

DOI: 10.1021/acs.energyfuels.5b01253
Energy Fuels 2015, 29, 6025−6038

characterize such samples, including micrometer- and submicrometer-scale spatial mapping of phases and element distributions using electron microprobe and micro-X-ray fluorescence (μ-XRF) imaging methods, as well as scanning electron microscopy (SEM) and transmission electron microscopy (TEM) coupled with energy dispersive X-ray analysis (EDAX). One of the most robust methods for determining metal speciation in solids is synchrotron-based X-ray absorption fine structure (XAFS) spectroscopy.[14,21,33,34,36−48] One type of XAFS spectroscopy that probes atoms at X-ray energies near their X-ray absorption edge—X-ray absorption near edge structure (XANES) spectroscopy—provides information on oxidation state and phase identity. Another type of XAFS spectroscopy that records modulations of an atom's absorption of X-rays up to 1000 eV above their X-ray absorption edge—extended X-ray absorption fine structure (EXAFS) spectroscopy—provides information on the identity, number, and distance of neighboring atoms around the absorbing atom. Both methods have been used extensively to determine the speciation of Hg in a variety of solid matrices.[21,38−52] Although XAFS spectroscopy has been used to determine the molecular-level speciation of As, Se, Ni, and Cr in coal fly ash samples,[33−36] it has not been widely used to determine the speciation of Hg in coal fly ash. The present study used XAFS spectroscopy and the imaging methods listed previously to determine (1) the size fractions of coal fly ash with which Hg is associated, (2) the solid phases and elements associated with Hg, and (3) the molecular-level speciation of Hg in the coal fly ash. Our results provide insights about the complexity of Hg speciation in coal fly ash as well as insights about the stability of Hg in the fly ash.

EXPERIMENTAL SECTION

Fly Ash Filtration. Fly ash was collected from a Kentucky utility pulverized-coal combustion unit burning a high-S coal blend. The sample was taken from an individual first-row electrostatic-precipitator (ESP) hopper. Two sizes of the same fly ash were used for this study: $\leq$0.1 μm and bulk ash. Our primary focus in this study was on particle sizes $\leq$0.1 μm because they have high surface areas per unit mass and thus can serve as effective sorbents of Hg and other heavy metals and in some systems can escape into the atmosphere, potentially transporting sorbed Hg into surrounding ecosystems. Additionally, fine ($\leq$0.1 μm) particles have been shown to cause greater pulmonary inflammation than coarser particles, with their surface properties contributing to their toxicity.[53] Because of their high surface area per unit mass, fine ash particles would also have a higher affinity for Hg uptake than larger ash particles. Four types of samples were used in this study: bulk fly ash (hereafter referred to as bulk ash) that was either not reacted or reacted with a simulated flue gas stream, and fine fly ash ($\leq$0.1 μm) that was either not reacted or reacted with the gas stream. The bulk ash was used as delivered with no additional manipulation of the samples.

Particle size separation to a final particle size of $\leq$0.1 μm was completed by suspending the fly ash in doubly deionized (DDI) water at a solid-to-solution ratio of ~1:60 and filtering the solutions using a 0.1 μm polycarbonate (VCTP) Millipore filter. Nonaqueous methods, such as microorifice and low-pressure impactors, are typically employed to handle dilute samples for air monitoring, rather than functioning as a bulk separation method, making them impractical for fly ash separation. Recent work by Lieberman et al.[54] showed very minor changes to the ash particles in a 1:40 solid:DDI water suspension relative to unreacted ash. The changes detected in that study were the leaching of Ca, SO_3, Na, and K, whereas all other elements analyzed showed no detectable change in concentrations in such suspensions. That study also found that the dominant ion leached from the fly ash was Ca, primarily the result of dissolution of the major Ca-containing phase—lime (CaO); the total amount of lime prior to DDI exposure was 9.5 wt % and after DDI washing was 8.5 wt %.[54] The other major elements leached were S, Na, and K and, though not stated by the authors, are most likely from the dissolution of gypsum or anhydrite found in nearly all coal fly ash.[26,28] SEM imaging coupled with EDAX of fly ash samples before and after exposure to DDI water showed no variations in particle morphology or major compositional changes in the glassy particles, iron oxides, and carbon-containing particles in the coal fly ash.[54] The only significant morphological and chemical changes were seen with the removal of some of the lime and presumably gypsum/anhydrite. Synchrotron-based X-ray photoelectron spectroscopy (XPS) studies of the interaction of low partial pressures of water vapor with several mineral phases commonly found in coal fly ash (α-Fe_2O_3, α-Al_2O_3;[55] Fe_3O_4[56]) showed that even at low partial pressures of H_2O vapor ($<10^{-4}$ Torr for MgO and α-Fe_2O_3), the mineral surfaces are fully hydrated. In the case of iron oxide surfaces, at partial pressures of 10^{-5} Torr H_2O, the surfaces of both hematite and magnetite are similar to those of the minerals in bulk water.[55,56] Another XPS study of lime (CaO) showed that the surface is also fully hydrated at very low H_2O partial pressures ($<10^{-9}$ Torr).[57] Once the surfaces of metal oxides become hydroxylated, it is difficult to remove the adsorbed water. For example, removal of water dissociated on MgO surfaces requires temperatures $\geq$ 750 °C.[58] Because the coal fly ash samples in our study had a moisture content of 0.94% at the time of collection, we assume that the surface hydration of iron oxides and similar minerals in the gas stream of a first-row electrostatic precipitator is similar to that of the fly ash minerals in contact with DDI water, based on the preceding XPS studies.

The $\leq$0.1 μm fraction was separated by first suspending the ash in DDI water and filtering the suspension through 0.2−0.6 μm glass microfiber (GMF) Millipore filters into clean 50 mL polypropylene centrifuge tubes. The filtrate was then refiltered through a 0.1 μm polycarbonate (VCTP) Millipore filter into another set of 50 mL polypropylene centrifuge tubes. The tubes were then placed in an oven set at 90 °C to volatilize the water. During filtration it was determined that the $\leq$0.1 μm fraction comprises <0.01% of the total fly ash (by weight); because of this low concentration, it was necessary to add a new filtered solution to the tubes containing the $\leq$0.1 μm fraction in order to concentrate this size fraction. During the filtration process, a total of 24 tubes of the $\leq$0.1 μm fraction were used, and the solid material was further consolidated into a single tube for additional cleaning. While drying, a white precipitate formed in the tubes. XRD analysis of the precipitate showed that the material is gypsum ($CaSO_4{\cdot}2H_2O$).

This separation technique was chosen because the DDI water should cause little alteration of the surfaces of unburned organics, aluminosilicate minerals, and glassy particles in the fly ash, as discussed earlier. In addition, following combustion, coal fly ash in a power plant is in contact with water vapor in the flue gas stream. In contrast, the DDI water did dissolve the calcium sulfate phases and lime in the main ash, which released sulfate, as well as alkaline earth and alkali metals, and subsequently precipitated these constituents as sulfate-bearing cementitious phases as well as gypsum. Based on the extremely low affinity between Hg and these constituents, there will be little to no impact on the uptake and speciation of Hg on the ash particles under simulated conditions of flue gas emission.[59] Total Hg analysis of the sulfate precipitate shows that it is not associated with Hg. Because Hg has a very low binding affinity to sulfate ($10^{1.34}$) and is not known to bind appreciably to gypsum,[59] removing the white precipitate from the filtered ash should not affect the speciation of Hg after the ash is reacted with a Hg-containing simulated coal-fired power plant flue gas exhaust stream. To remove gypsum from the samples, the consolidated ash from the 50 mL polypropylene tubes was placed in a 250 mL acid-washed centrifuge tube and filled to approximately two-thirds volume with DDI water. The tube was agitated for several minutes to dissolve the gypsum crystals and was then centrifuged at 10000 rpm for 1 h, and the supernatant was removed, taking great care not to remove any ash material. This cleaning process was done five additional times to remove the majority of the gypsum from the sample. After cleaning, the tube was placed in the 90 °C oven to dry. Once dry, the ash was ground in an agate mortar and pestle to disaggregate the sample as much as possible. SEM imaging of the filtered material confirmed that the ash particles were $\leq$0.1 μm in size. XRD analysis of the ash indicated that there was still a small amount of gypsum present in the sample (~15 wt %), which is

DOI: 10.1021/acs.energyfuels.5b01253
Energy Fuels 2015, 29, 6025−6038

similar to coal-fired power plant systems where gypsum is present in the fly ash. Mercury analysis of the removed gypsum showed no detectable Hg.

Packed-Bed Hg Exposure. A packed-bed reactor (PBR) system was configured to expose fly ash samples to a methane-combustion flue gas containing Hg in order to evaluate the interaction of Hg with fly ash particle surfaces. The flue gas is created through the combustion of 99.0% methane with medical-grade compressed air, which produces a stable flame and a laminar flow regime with a total flow rate of 2.2 L/min. Stoichiometric ratios of N_2 (72%), CO_2 (8%), and H_2O vapor (16%) are formed from the combustion reaction, with an O_2 content of approximately 3%. HCl was also included in the combustion reaction, at 50 ppmv, in order to simulate potential reactions in the coal boiler. Desired amounts of NO (300 ppmv), NO_2 (5 ppmv), and SO_2 (300 ppmv) were mixed downstream of the flame, but upstream of the packed bed. Flue gas from methane combustion has previously been used as a stand-in for coal-combustion flue gas to study the interactions of Hg with brominated activated carbon fibers.[21,60] All gases were obtained from Praxair and controlled with Brooks Instrument 5850E mass flow controllers, except for air, which was controlled by the PS analytical 10.356 Mercury calibration system. Elemental mercury was added precombustion, also through the 10.356 Mercury calibration system, at a concentration of 580 $\mu g\ m^{-3}$. The Hg concentration is 100× higher than that of a typical coal-fired flue gas in order to facilitate adsorption and increase surface concentration for the analytical X-ray techniques we used to characterize the molecular-level speciation of mercury. Although the maximum adsorption capacity of some materials can vary, including activated carbons loaded with sulfur compounds, there is no indication that the chemisorption mechanism changes at higher loadings.[61] Packed beds of 50 mg ±1.1 mg of the fly ash material were supported in a 7 mm o.d. quartz reactor maintained at 140 °C by a Carbolite tube furnace. Each sample was exposed to the flue gas for 240 min with a total exposure to 6.2 mg of Hg/(g of fly ash).

XRD, XRF, CVAFS, and FTIR Analyses. All fly ash samples were analyzed using powder X-ray diffraction (XRD) to identify the major crystalline phases present in the samples. X-ray diffractograms were collected on a Rigaku model CM2029 powder X-ray diffractometer using a Cu Kα X-ray source over the 2θ range of 5−70°, and the data were analyzed using JADE diffraction software.[62] Peak identification was accomplished by matching the four most intense diffraction peaks for a given phase to those of the mineral phases in the National Institute of Standards and Technology (NIST) database. A few X-ray diffractograms of the filtered samples, both reacted and unreacted, were collected using Laue diffraction at beamline 11-3 at SSRL at an X-ray energy of 12724.98 eV. Pattern conversion was completed using the Area Diffraction Machine software,[63] over a 2θ range of 3.5−60°. The converted patterns were analyzed using JADE diffraction software[62] and the same rubric as stated earlier.

Total elemental compositions were measured using XRF analysis in the Stanford Environmental Measurements Laboratory. The bulk and filtered ash materials were analyzed using a Spectro Analytical XRF model XEPOS HE. A standard reference material, NIST SRM 1633c (coal fly ash), was analyzed in addition to our ash samples to confirm the accuracy of the technique. Samples were analyzed prior to reaction in the packed bed reactor. Results for the NIST standard indicate that the XRF technique was not accurate for Hg, Ba, S, and Cd.

To accurately determine total Hg concentrations for the unreacted bulk ash, unreacted fine ash, reacted bulk ash, and the reacted fine ash, acid digestions followed by cold vapor atomic fluorescence spectrometry (CVAFS) analysis were carried out. Samples were dissolved in aqua regia (8 mL of HCL to 2 mL of HNO_3, preserved with 0.5% BrCl), and total Hg was determined using a Tekran 2600 series CVAFS following EPA method 1631.[64] Total Hg recovery for the NIST SRM 1633c sample was 107%, illustrating the validity of this technique for total Hg concentrations in coal fly ash.

Fourier transform infrared (FTIR) spectroscopy on the fly ash (both filtered and unfiltered) before and after reaction in the simulated flue gas stream was used to identify organic functional groups and organic molecules present in the samples and to help determine which, if any, functional groups reacted with Hg in the fly ash. Due to the high amount of Fe in the sample pellets made for transmission FTIR analysis, the pellets were composed of 0.005 g of sample diluted in 0.1 g of FTIR-grade KBr. The sample chamber was purged with N_2 for 30 min prior to collection of spectra to minimize absorption signals from the presence of water vapor and CO_2. FTIR spectra were collected using a Nicolet Nexus model 470 FT-IR, with a resolution of 1 cm^{-1} over a frequency range of 400−4000 cm^{-1}. A total of 1000 scans in transmission were collected for each sample, and these data were subsequently converted to total absorbance. Peak identification was done using Nicolet peak identification software along with tables for IR absorbance bands for various functional groups.[65−69]

Computational Simulations of FTIR Spectra. *Ab initio* electronic structure calculations were performed on two isolated dehydrated molecules—$OHCH_2COOH$ and $OHCH_2COOHgOH$—using the density functional theory (DFT) code, CASTEP,[70] employing a plane wave basis set and pseudopotentials within the DFT formalism.[71−73] The valence electron wave functions were expanded in a plane wave basis set represented by a kinetic energy cutoff of 830 eV. The electron−ion interactions were described by norm-conserving, Perdew, Burke, and Ernzerhof (PBE) pseudopotentials generated by Opium.[74,75] These pseudopotentials were consistent with the description of the exchange-correlation effects by the generalized gradient approximation (GGA) density functional, specifically (GGA)PBE.[76] The (geometry) optimizer was Broyden−Fletcher−Goldfarb−Shanno (BFGS),[77] and the electronic structure minimization method was density mixing. The Brillouin zone integrations were performed at the γ point for both molecules, each contained within a 20 Å × 20 Å × 20 Å cube. The electronic energy tolerance was 5×10^{-7} eV, and the maximum force was converged to $|F|_{max}$ = 0.01 eV/Å. All calculations were non-spin-polarized, and the models were created and visualized using Materials Studio.[78] Following geometrical equilibration of atomic positions, the vibrational frequencies were calculated using density functional perturbation theory (DFPT).[79]

X-ray Spectroscopy. Samples were analyzed on two separate beamlines at the Stanford Synchrotron Radiation Lightsource (SSRL). The unreacted and reacted samples were first analyzed using synchrotron-based μ-XRF mapping and μ-XANES spectroscopy on beamline 2-3 at SSRL. Beamline 2-3 is a bending magnet beamline that uses two water-cooled Si(111) monochromator crystals in the ϕ = 90° orientation. Data were collected using a three-element vortex detector in fluorescence mode. The μ-XRF mapping energy was set to 14 keV with a 2 μm × 2 μm beam size and a detection limit of approximately 50 ppm for each element per pixel. In Hg hot spots identified by μ-XRF mapping, Hg L_{III}-edge μ-XANES spectra were collected from 230 eV below to 330 eV above the Hg L_{III}-edge (12 284 eV). Energy calibration was done using a $HgCl_2$ foil placed behind the I_1 detector. Descriptions of data analysis for μ-XRF and μ-XANES data are given later.

Mercury L_{III}-edge EXAFS spectra for the filtered, reacted fly ash sample were collected on SSRL beamline 11-2. Beamline 11-2 has a wiggler insertion device and uses two water-cooled Si(220) monochromator crystals in the ϕ = 90° orientation. Data were collected in fluorescence mode using a Canberra 100-element Ge detector. A $HgCl_2$ foil was inserted between the second and third ion chambers for continuous energy calibration. The samples were cooled in a LN_2 cryostat during EXAFS data collection to reduce thermal disorder following the slow-cooling method outlined by Jew et al.,[39] which was used to detect elemental Hg, if present, in the sample. A total of 15 scans were collected for the filtered, reacted fly ash sample, with a maximum k-range of 14 $Å^{-1}$.

The μ-XRF maps were processed and analyzed using SMAK,[80] and μ-XANES and EXAFS spectra were analyzed using SixPACK.[81,82] The μ-XANES spectra were fit by linear combination fitting (LCF) of spectra collected for various Hg-containing reference compounds. XANES data were fit from 100 eV below to 330 eV above the Hg L_{III}-edge. Goodness of fit was determined by calculating the residual of the fit using one-component or multicomponent fits. Fitting of the EXAFS spectra was done using the shell-by-shell technique with theoretical scattering pathways derived from crystallographic data and FEFF 6L software.[83] Goodness of fit was determined by examining both the reduced χ^2 and the R-factor. For each pathway added to the shell-by-shell fit, an R-factor

DOI: 10.1021/acs.energyfuels.5b01253
Energy Fuels 2015, 29, 6025−6038

Table 1. Concentrations of Selected Oxide Components and Elements for the Bulk Fly Ash and the Fine (<0.1 μm) Fly Ash Fraction before and after Reaction with the Simulated Flue Gas Stream[a]

sample	unreacted bulk	reacted bulk	unreacted fine	reacted fine
% ash	98.11	98.11	83.31	83.31
% moisture	0.95	0.95	N/A	N/A
% carbon	0.68	0.68	4.01	4.01
% hydrogen	0.08	0.08	N/A	N/A
% total sulfur	1.5	1.5	N/A	N/A
% SiO_2	48.77 ± 0.08	48.77 ± 0.08	0.15 ± 0.01	0.15 ± 0.01
% Al_2O_3	26.04 ± 0.07	26.04 ± 0.07	0.004 ± 0.001	0.004 ± 0.001
% Fe_2O_3	11.9 ± 0.1	11.9 ± 0.1	13.7 ± 0.1	13.7 ± 0.1
% CaO	4.56 ± 0.01	4.56 ± 0.01	14.7 ± 0.1	14.7 ± 0.1
% MgO	1.03 ± 0.02	1.03 ± 0.02	<3 ppm	<3 ppm
% Na_2O	0.53 ± 0.03	0.53 ± 0.03	<3 ppm	<3 ppm
% K_2O	2.4 ± 0.01	2.4 ± 0.01	5.24 ± 0.01	5.24 ± 0.01
% P_2O_5	0.40 ± 0.01	0.40 ± 0.01	0.26 ± 0.01	0.26 ± 0.01
% TiO_2	1.09 ± 0.02	1.09 ± 0.02	<3 ppm	<3 ppm
ppm of Cr	191 ± 1	191 ± 1	24 ± 1	24 ± 1
ppm Mn	299 ± 1	299 ± 1	195 ± 1	195 ± 1
ppm of Ni	147 ± 2	147 ± 2	96 ± 1	96 ± 1
ppm of Cu	297 ± 2	297 ± 2	122 ± 1	122 ± 1
ppm Zn	687 ± 3	687 ± 3	321 ± 1	321 ± 1
ppm As	155 ± 1	155 ± 1	116 ± 1	116 ± 1
ppm Pb	241 ± 3	241 ± 3	2.5 ± 1.1	2.5 ± 1.1
ppm of Cl	11 ± 1	11 ± 1	42 ± 1	42 ± 1
ppm of Se	0.6 ± 0.2	0.6 ± 0.2	2.0 ± 0.2	2.0 ± 0.2
ppm Br	<0.3	<0.3	10.2 ± 0.2	10.2 ± 0.2
ppm of Hg	0.011 ± 0.008	0.164 ± 0.004	0.100 ± 0.006	610 ± 20

[a]N/A = not available.

ratio test[84] was conducted to verify that the improvement to the fit caused by the addition of another scattering pathway was statistically significant.

SEM and Microprobe Analyses. Scanning electron microscopy and electron microprobe analysis were carried out at the Stanford Nanocharacterization Laboratory. Both filtered and unfiltered samples were analyzed using a Sirion model FEI XL30 SEM to determine particle size and shape. Powdered samples were mounted using conductive glue and were gold−paladium coated to increase sample conductivity. The filtered fly ash material was analyzed before and after reaction with the simulated flue gas stream to determine if aggregation or particulate coarsening occurred.

A major limitation of μ-XRF analysis done in air is the inability to detect fluorescence from light elements such as C, O, and N due to X-ray photons being scattered and attenuated by air prior to reaching the detector. Because of this limitation, samples were analyzed using a JEOL model JXA-8230 SuperProbe electron microprobe to determine if there is any correlation between Hg and C, both unburned and residual, in the fly ash. Powdered samples were suspended in DDI water, and several drops of the suspended material were placed on a microscope slide. After drying, the slides were carbon coated to increase sample conductivity and limit charging effects. The C coating of the sample is of sufficient thinness that it is undetectable in the electron microprobe, while C detected in the microprobe is solely from the sample. Spatial resolution for the analysis was approximately 3 μm, with a minimum detection limit of approximately 500 ppm for elements Be to F and 300 ppm for elements Na to U.

RESULTS

Fly Ash Characterization. The particle sizes determined by SEM imaging in the unfiltered fly ash were between 20 nm and 10 μm in diameter. SEM imaging of the filtered material confirmed that all of the ash particles are ≤0.1 μm in diameter (data not shown). A selection of the elemental analysis results for the ash (bulk and fine fraction) is shown in Table 1. Laboratory-based XRF analysis of the NIST fly ash standard indicates that most of the elemental concentrations are within 10% of the NIST-certified values. However, the concentrations of four elements (S, Ba, Cd, and Hg) analyzed in the NIST standard are significantly lower than the NIST-certified values (S is 37-fold lower, Ba is 25% lower, Cd is 90% lower, and Hg is 4-fold lower). Because of the poor accuracy of XRF for total Hg concentrations, acid digestions followed by cold vapor atomic fluorescence spectrometry (CVAFS) analyses were done on the fly ash samples. Analysis of the NIST fly ash standard using this method resulted in good accuracy with 107% recovery of Hg when compared to the certified values. The Hg concentrations of the unreacted bulk ash were low with a concentration of 11 ± 0.8 ppb. In contrast, the unreacted fine ash has a concentration of 100 ± 6 ppb (Table 1). After reacting the ash with the simulated flue gas stream, the total Hg concentrations showed an increase of approximately an order of magnitude for the reacted bulk ash with a concentration of 164 ± 4 ppb, whereas the reacted fine ash Hg concentration is 610 ± 20 ppm (Table 1), which represents an increase of over 3 orders of magnitude with respect to the bulk ash. Synchrotron-based XRD analysis of the bulk fly ash indicates that the majority of the ash is amorphous. Only quartz (α-SiO_2) and hematite (α-Fe_2O_3) were identified as crystalline phases in the bulk fly ash. In the fine fraction (≤0.1 μm), the main crystalline phases detected were quartz, hematite, gypsum ($CaSO_4 \cdot 2H_2O$), and one or more of three different evaporite-based cementitious phases: syngenite ($K_2Ca(SO_4)_2 \cdot H_2O$), glauberite ($Na_2Ca(SO_4)_2$), and picromerite ($K_2Mg(SO_4)_2 \cdot 6H_2O$). Because of the similarity of lattice parameters of these three phases and the presence of K, Na, Ca, and Mg in the fine fraction fly ash sample, it is impossible to differentiate among these cementitious phases by XRD. The presence of one or more

DOI: 10.1021/acs.energyfuels.5b01253
Energy Fuels 2015, 29, 6025−6038

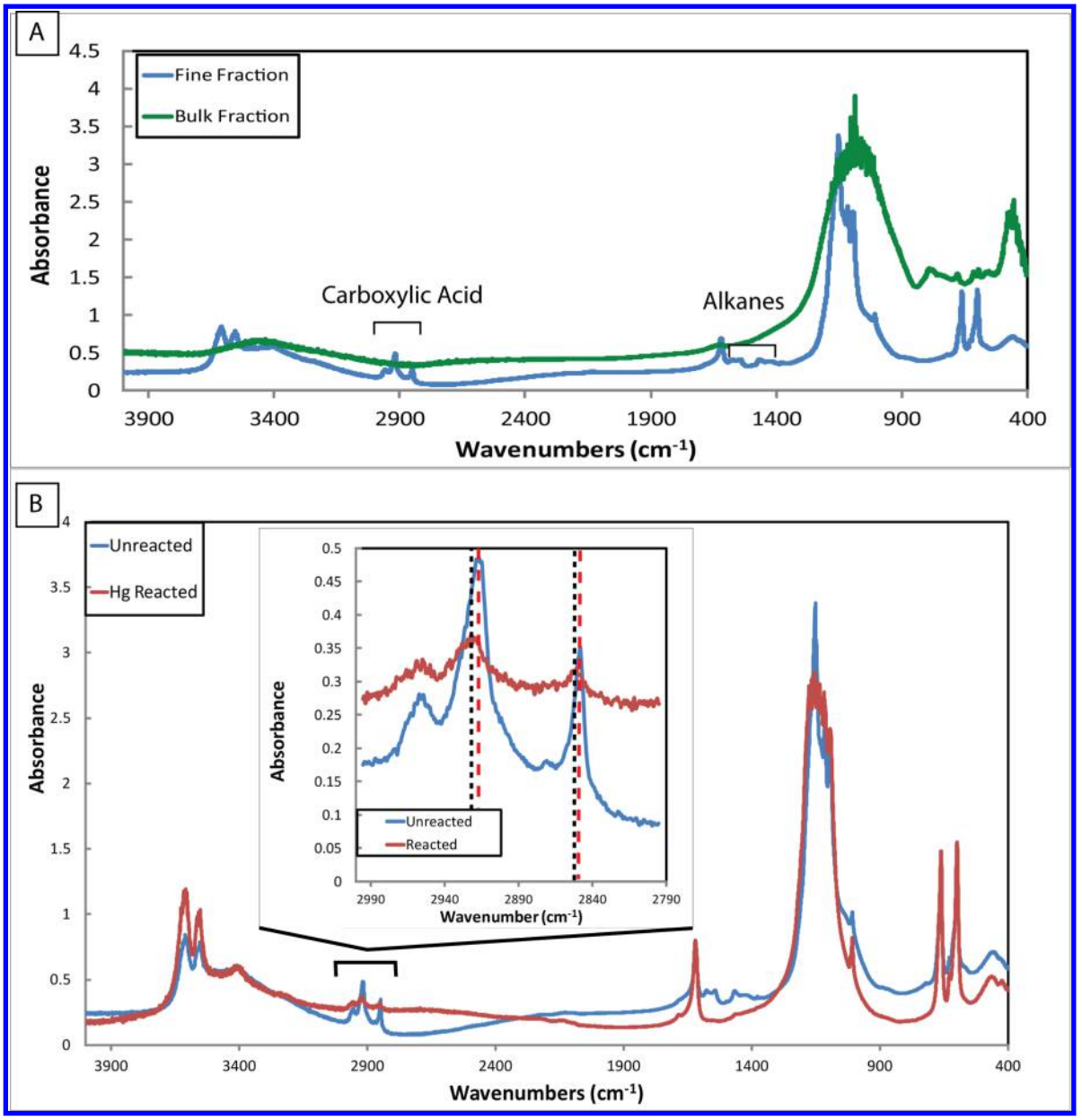

Figure 1. FTIR spectra for fly ash samples. (A) FTIR spectra for unreacted bulk and unreacted fine fly ash. Brackets denote the regions of the spectra that indicate carboxylic acid functional groups and alkane chains. (B) FTIR of fine ash material before and after reaction with simulated flue gas stream. There is a higher intensity of all peaks, but the carboxylic acid functional groups are due to background removal of sample spectra. Spectra for reacted fine fly ash indicate that the flue gas stream is reacting with the carboxylic acid functional groups as well as the alkane chains found in the organic material. Inset in B shows the FTIR spectra focusing on the carboxylic acid functional groups around 2900 cm^{-1} illustrating a peak shift of 2 and 3 wavenumbers which is consistent with theoretical calculations for Hg binding to a carboxylic acid functional group.

of these three cementitious phases in the fly ash sample prior to reaction with the simulated flue gas stream is due to their initial dissolution during suspension of the fly ash in DDI water and precipitation of the cements during the drying process. The only detectable difference in the diffractograms of the fine ash fraction before and after reaction is the presence of anhydrite ($CaSO_4$) following reaction. This difference is due to partial transformation of gypsum crystals to anhydrite when the ash was reacted with the simulated flue gas stream at ~140 °C. As particle size decreased, the amount of iron oxide phases present in the ash increased.

Analysis of the ash by FTIR spectroscopy showed significant differences between the unfiltered and filtered (both unreacted) fly ash material, especially in the higher wavenumber regions, which are generally associated with organic functional groups (Figure 1A). The FTIR spectrum of the unreacted bulk ash had very little structure from 1400 to 4000 cm^{-1}, whereas that of the unreacted fine ash sample had three major regions in the same wavenumber range with structure. The main FTIR absorption feature in the unreacted bulk ash sample is not seen in the unreacted fine ash (Figure 1A) and is most likely due to the unidentified amorphous phases detected in the X-ray diffractogram. The unreacted fine ash sample showed significant adsorption bands in the following spectral regions: 3350−3680 cm^{-1} (generally associated with alcoholic functional groups), 2820−2995 cm^{-1} (associated with carboxylic functional groups), and 1350−1695 cm^{-1} (associated with alkanes). For both filtered samples, most of the FTIR absorption bands are associated with

DOI: 10.1021/acs.energyfuels.5b01253
Energy Fuels 2015, 29, 6025−6038

gypsum that precipitated following sample drying (Figure 1B). The strong contribution to the FTIR spectra by gypsum is consistent with gypsum detected in the XRD patterns of the same samples. Below 1350 cm^{-1}, there are fewer differences between the FTIR spectra of the unreacted bulk and unreacted fine fly ash samples. Comparison of the FTIR spectra of the unreacted fine and the reacted fine ash samples (Figure 1B) shows that the absorption peaks in the reacted fine ash sample are more intense. This difference is due to the use of a different blank spectrum in processing the sample spectra. In all FTIR spectral regions except for that dominated by carboxylic functional groups (2848 and 2917 cm^{-1}), the peak intensity for the reacted fine ash sample is greater than that of the unreacted fine ash sample. However, there is a significant decrease in the intensity of these absorption bands as well as a two wavenumber shift of the peaks to a higher energy for the peak at 2848 cm^{-1} and a three wavenumber shift for the peak at 2917 cm^{-1} (Figure 1B). The results of DFT calculations simulating the vibrational frequencies and peak intensities for Hg binding to a carboxylic functional group are consistent with the experimental FTIR data. In addition, the DFT results also show a decrease in absorption peak intensity. Further evidence for a possible association between C and Hg is seen in the electron microprobe data (Figure 2A,B), which show that in certain areas there is no association between Hg and C, whereas in other areas there is a strong association. These results suggest that Hg binds to the carboxylic acid functional groups contained in the carbon-rich regions of the fly ash.

μ-XRF and μ-X-ray Absorption Fine Structure Spectroscopic Analyses. The synchrotron-based Hg μ-XRF maps for the unreacted bulk ash show significant iron in areas where sample thickness is sufficient ($\geq$0.1 mm) to produce a strong fluorescence signal (Figure 3A). Although a few Hg hot spots were detected, in general the unreacted ash has little Hg, and Hg does not correlate spatially with Fe in the unreacted bulk ash sample (Figure 3A,B). However, Hg was detected in this sample in small Hg-rich hot spots but was not correlated spatially with other transition metals, including Ti, V, Cr, Mn, Fe, Co, Ni, Cu, and Zn. Synchrotron-based μ-XRF maps of the reacted bulk fly ash show little difference relative to maps of the unreacted bulk fly ash (Figure 3C), and there is no spatial correlation between Fe and Hg in these samples (Figure 3C,D). The Hg hot spots identified in the μ-XRF maps of the unreacted bulk ash were too low in concentration to analyze using μ-XANES techniques. When the μ-XRF maps of the reacted bulk ash (Figures 3C,D) are compared with those of the reacted fine ash, they show that the finer fraction ($\leq$0.1 μm) has more evenly dispersed Fe and sorbs more Hg than the bulk material (Figure 4A,B). The reacted fine ash had sufficient Hg levels (610 $\pm$ 20 ppm) to produce EXAFS spectra that could be analyzed. As shown in the μ-XRF map for the reacted fine ash, Hg occurs dominantly in two types of regions: Hg associated with Fe and Hg hot spots not associated with Fe (Figure 4B). SEM analyses of ash samples following reaction show that the fine fly ash fraction coarsens or is aggregated by the sulfate-based cements, explaining why the Hg hot spots and Hg associated with Fe-rich regions are much larger than the $\leq$0.1 μm seen by SEM following filtration. Finer resolution maps of the Fe-associated Hg regions show clear associations of Fe (Figure 4C), Hg (Figure 4D), and Cl (Figure 4E). Also in the Fe-associated regions, Hg is correlated with Fe as seen in the Hg/Fe correlation plot (Figure 4E). There is a slight spatial correlation ($r^2 < 0.6$) between Hg and other metals (Ti, Mn, Zn, Cr, Cu, and Ni), but this is more likely due to the metals being associated with Fe instead of with Hg. In finer resolution maps, Hg hot spots are ~10 μm × 20 μm in size and show no correlation with Fe (Figure 5A,B). Hg in the hot spots is highly correlated with Br, however (Figure 5C), and moderately correlated with As and Se (data not shown). Due to the limited energy range of SSRL beamline 2-3, which does not extend down to the S K-edge (~2472 eV), acceptable sulfur μ-XRF maps could not be collected on the same samples used for imaging the distribution of the heavier elements. The Hg hot spots in the reacted fine ash did contain sufficient concentrations of Hg to produce Hg L_{III} μ-XANES spectra that could be analyzed. Linear

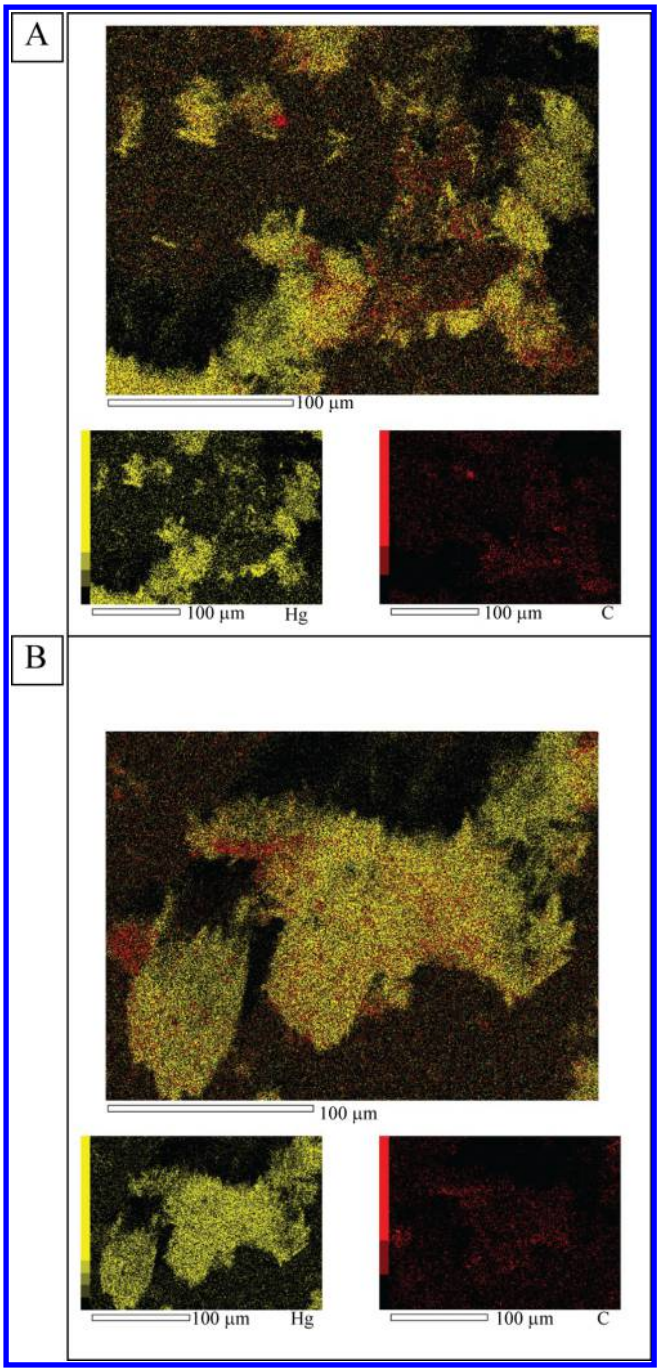

Figure 2. Electron microprobe images of reacted fine fly ash. (A) Bicolor image showing little correlation between Hg and C in certain regions of the sample. (B) Bicolor image showing high correlation between Hg and C in different regions of the same sample.

DOI: 10.1021/acs.energyfuels.5b01253
Energy Fuels 2015, 29, 6025−6038

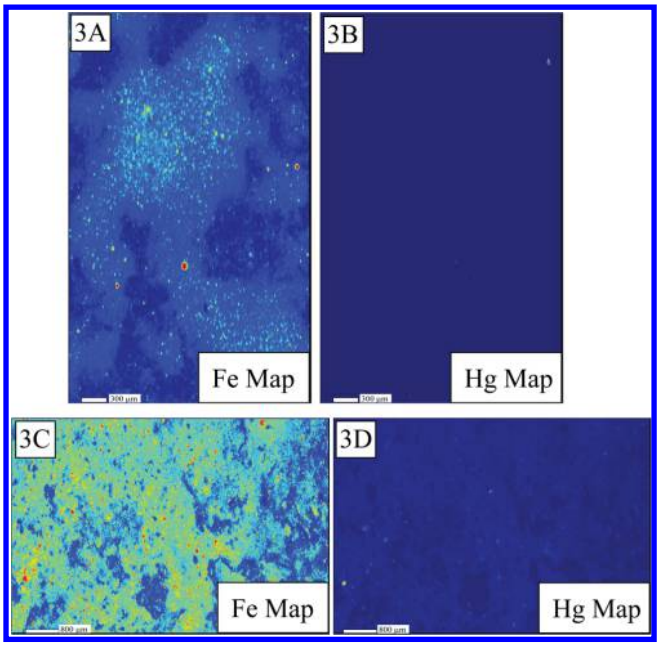

Figure 3. μ-XRF maps of bulk fly ash samples. (A) Fe map of unreacted bulk fly ash. Dark regions of the map are areas of low sample coverage on the sample holder. (B) Hg map of the same region from panel A. (C) Fe map of reacted bulk fly ash sample. Stronger Fe signal is due to better sample coverage on the Kapton tape sample holder. (D) Hg map for the same region as that in panel C. Panels A and B show little Hg in the unreacted bulk fly ash sample and little to no correlation with Fe, while panels C and D show some Hg uptake that is correlated with the Fe along with Hg hot spots not associated with Fe.

combination fitting of the μ-XANES spectrum of the reacted fine ash using reference spectra for cinnabar (α-HgS), metacinnabar (β-HgS), tiemannite (HgSe), montroydite (HgO), $HgSO_4$, calomel (Hg_2Cl_2), $HgCl_2$, schuetteite ($Hg_3O_2(SO_4)$, corderoite ($Hg_3S_2(Cl,Br)_2$, eglestonite ($HgHCl_3O_2$), kleinite ($Hg_2N(Cl,SO_4)\cdot nH_2O$), and α-Hg^0 indicates that the main phase present in the reacted fine ash is cinnabar (Figure 6), with no evidence for the other Hg species in the Hg hot spots.

Analysis of Bulk XAFS Spectra. Analysis of the XANES region of the X-ray absorption fine structure spectrum of the slowly cooled sample indicates that the bulk of the Hg in the sample is in the Hg^{2+} oxidation state with no detectable elemental Hg in the form of α-Hg^0.[39] The EXAFS spectrum collected for the reacted fine ash is highly complex, indicating the presence of up to six individual scattering pathways (Figure 7A). Wavelet analysis[85] (data not shown) indicates that the features in the Fourier transform to a distance of 3.2 Å (Figure 7B) are real, whereas the features at greater distances are artifacts. Shell-by-shell fitting of the data was done by fitting the shortest scattering pathway first, optimizing the fit, then adding the next shortest pathway, optimizing the fit, and so on until the addition of scattering pathways either made the fit worse or did not result in a statistically significant improvement. In total, six pathways were needed to properly fit the data (Table 2). The pathways included two Hg−O pathways, one Hg−Cl, one Hg−S, one Hg−Br, and one Hg−Fe pathway. The two different Hg−O pathways have different interatomic distances, indicating one species with two different Hg−O distances or two different Hg−O species. Fitting of the EXAFS spectrum of the reacted fine ash indicates that the shortest pathway is Hg−Cl with a distance of 1.75 ± 0.01 Å, followed by Hg−O at 1.82 ± 0.01 Å, Hg−S at 2.36 ± 0.01 Å, another Hg−O at 2.65 ± 0.02 Å, Hg−Br at 2.77 ± 0.01 Å, and a final Hg−Fe pathway at 3.09 ± 0.01 Å (Table 2). Given the high number of pathways involved in the fit, the coordination number of each Hg species detected is not considered to be of high accuracy due to the destructive and constructive interference among all six pathways. Though FTIR, microprobe, μ-XRF, and μ-XANES data support the use of all of these pathways in fitting the bulk EXAFS data, a statistical test is necessary to support the addition of all six pathways. To statistically test whether the addition of each pathway is statistically significant, Hamilton's *R*-factor ratio test[84] was performed as each pathway was added to the fit. All pathways added to the fit passed the *R*-factor ratio test at the 99.5% confidence level (Table 3), indicating that they are statistically significant.

DISCUSSION

The ≤0.1 μm fraction makes up a very minor part (~0.01% by weight) of the total fly ash. Even though SEM images show that the filtered ash particles have a diameter of ≤0.1 μm prior to reaction in the packed-bed reactor, SEM, electron microprobe, and μ-XRF all indicate that the particles coarsen during the reaction process. This coarsening is most likely due to the elevated temperature early in the combustion stream causing gypsum particles to dehydrate throughout the reaction process, followed by Ostwald ripening as water is added to the combustion stream, resulting in an increase in particle size. Although the fine fraction comprises only a minor fraction of the total ash, total Hg concentrations (Table 1) and μ-XRF analysis of the fly ash before and after reaction show that the fine ash fraction (≤0.1 μm) dominates the uptake of Hg from the simulated flue gas stream (Figures 3D and 4B). In reacted bulk ash, Hg is present as a few small Hg hot spots not associated with Fe (Figure 3D). In contrast, the reacted fine ash also shows the presence of Hg hot spots, but the majority of Hg is associated with Fe-rich regions (Figure 4B).

FTIR and XRD analyses of the unreacted samples (bulk and fine) show significant differences (Figure 1A). The FTIR spectrum for unreacted fine ash shows the presence of numerous additional organic functional groups (primarily carboxylic acid, alcoholic, and single-bonded carbon chains) that are not detectable in the FTIR spectrum of the unreacted bulk sample. XRD analysis indicates that the majority of the amorphous material in the fly ash is in the >0.1 μm size fraction. XRD analysis also indicates that the dominant crystalline Fe-bearing phase present in all of the fly ash samples is hematite. Various K-, Na-, Mg-, Ca-, and sulfate-containing cementitious phases in the fine fraction are the result of the filtration process in conjunction with sample drying. Although XRD and FTIR analyses of the unreacted fine and reacted fine ash samples show a strong contribution from gypsum and sulfate-based cements, the gypsum and cements are not thought to be major adsorbents of Hg. The lack of an association of Hg with these sulfate-based phases is shown by XAFS analysis (detailed later) and is also consistent with the low binding constant of Hg to gypsum (log K = 1.34,[59]). The difference in FTIR spectra between the bulk and filtered ash samples indicates that as particle size decreases, the binding of Hg to the organic material in the ash increases. The FTIR peak positions and relative peak intensities are similar for the unreacted fine and reacted fine ash samples except for the 2820−2995 cm^{-1} region. The two absorption bands at 2848 and 2917 cm^{-1} are commonly attributed to carboxylic acid functional groups. After reaction of the fly ash with the Hg-containing simulated flue gas, the two carboxylic acid absorption peaks shift

DOI: 10.1021/acs.energyfuels.5b01253
Energy Fuels 2015, 29, 6025−6038

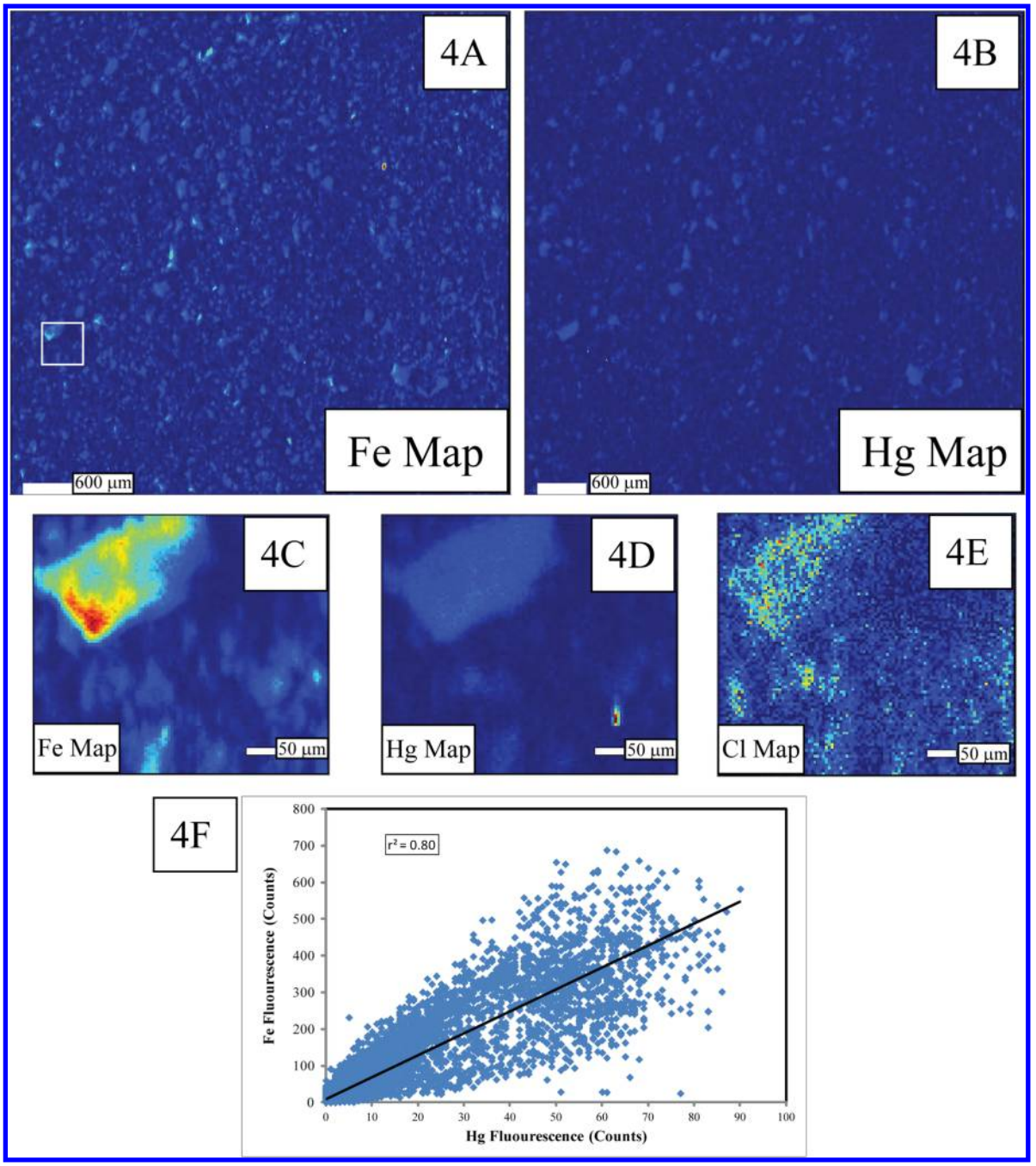

Figure 4. μ-XRF maps of reacted fine ash sample. (A) Large Fe fluorescence map. (B) Large Hg fluorescence map of the same region as that in panel A. (C) Fe fluorescence map of the boxed area denoted in panel A. (D) Hg fluorescence map of the boxed area showing Fe-associated Hg-rich areas and Hg hot spots. (E) Cl fluorescence map of the boxed area showing correlation between Cl and Fe. (F) Correlation plot of Fe fluorescence versus Hg fluorescence for the region in panel C excluding the Hg hot spot seen in the lower right corner of panel D.

two and three wavenumbers higher in energy (2848 and 2917 cm^{-1}, respectively). In addition, the absorption band intensities decrease significantly after reaction. DFT simulations of the vibrational frequencies of carboxylic acid functional groups before and after reaction with Hg were generated and compared with experimental frequencies and intensities. The simulations showed identical shifts in peak energy and a dampening in absorption intensity consistent with experimental data. The comparison between experimental and simulated vibrational frequencies suggests that Hg binds to carboxylic acid functional groups in the fly ash.

Analysis by μ-XRF of the fine fly ash fraction after reaction with the simulated flue gas stream provides important insights about the interaction of Hg with the fly ash. In certain areas of the sample there is a strong spatial correlation of Hg with Fe and Cl (Figures 4A–C). Although μ-XRF of the Fe-associated Hg shows some spatial correlation with other metals (Mn, Zn, K, Cr, Cu, and Ni, among others), these correlations are more likely due to the correlation between Fe and these metals instead of with Hg (data not shown). The μ-XRF data show no spatial correlation between Hg and the alkali metals, alkaline earth metals, and transition metals (except for Fe). The other major type of region where Hg is found is in ~10 μm × 20 μm Hg hot

DOI: 10.1021/acs.energyfuels.5b01253
Energy Fuels 2015, 29, 6025–6038

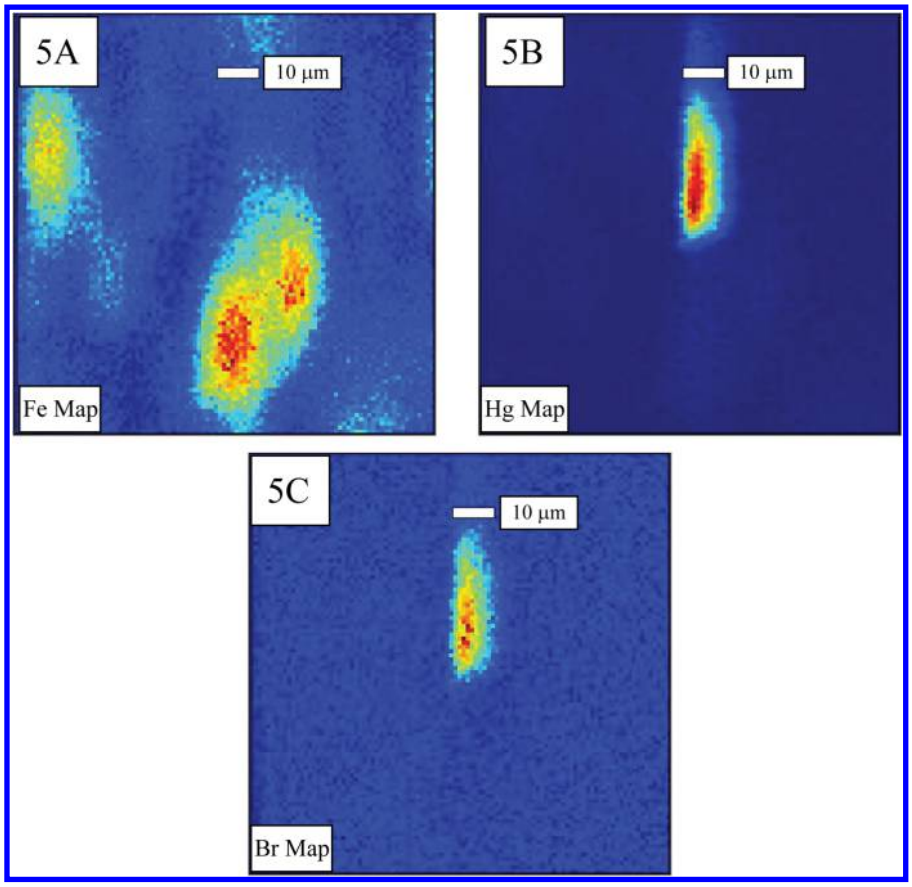

Figure 5. μ-XRF map of Hg hot spot in the reacted fine fly ash sample. (A) Fe fluorescence map of the Hg hot spot region. (B) Hg fluorescence map of the Hg hot spot showing no correlation between Fe and Hg. (C) Br fluorescence map showing a high correlation between Br and Hg in the Hg hot spots. As and Se also show a moderate correlation with Hg in Hg hot spots (data not shown).

spots that have no detectable Fe (Figure 5A,B). μ-XRF analysis of these Hg hot spots indicates significantly different elemental compositions compared to the regions where Hg is strongly associated with Fe, including a high spatial correlation between Hg and Br (Figure 5B,C), and a minor correlation of Hg with As and Se (data not shown). Additional elements detected in the Fe-associated regions (Mn, Zn, and Cl, etc.) were not detected in the Hg hot spots (Figure 5A). Although sulfur maps cannot be collected on SSRL beamline 2-3, μ-XANES confirms that the dominant phase comprising the Hg hot spots is cinnabar (α-HgS) (Figure 6), indicating that a portion of the S in the system is in the form of S^{2-}. Because the samples were not analyzed in a vacuum environment, the μ-XRF technique in air was unable to detect lighter elements such as N, C, and O. Electron microprobe analysis, which can detect C, was necessary to determine if there was any spatial correlation between Hg and organics in the fly ash samples. As seen in Figure 2A,B, there are regions in the reacted fine ash in which Hg and C show no clear spatial correlation (Figure 2A) and regions in which there are moderate correlations (Figure 2B). The correlation between Hg and C in some regions adds further support for the hypothesis that some of the Hg reacted with carboxylic groups in the filtered fly ash. The presence of cinnabar detected in the μ-XANES data for the hot spots indicates a strong correlation between Hg and S in specific regions of the samples.

Bulk EXAFS analysis of the reacted fine fly ash provides important information about the speciation of Hg in the fine fraction of the fly ash. The XANES region of the X-ray absorption fine structure spectrum indicates that Hg is dominantly in the Hg^{2+} state. The lack of α-Hg^0 in the reacted fine ash is confirmed by slow-cooling experiments in which any Hg^0 liquid or vapor present would be converted into crystalline α-Hg^0, which should be detectable in the EXAFS spectrum, assuming sufficient concentration.[39] Previous laboratory work with this specific packed-bed experimental reactor under similar conditions using a mass spectrometer to detect different gas-phase Hg species has shown no gas-phase, homogeneous oxidation of Hg. Because the gas stream does not oxidize Hg^0 under our experimental conditions, and the EXAFS analysis of a slow-cooled sample shows no detectable Hg^0 in the reacted fly ash, Hg oxidation appears to occur upon initial contact of the gas stream with the fly ash particles.

The shell-by-shell EXAFS fitting results illustrate the highly complex nature of Hg speciation in the fine fly ash fraction. Though principle component analysis (PCA) is often used to determine the total number of pathways needed to fit a sample, due to the complexity of the sample, reference spectra for all types of Hg species required for this data set were not available, thus making PCA impractical. A total of six different pathways were fit to the data, with the shortest being a Hg−Cl pathway with a distance of 1.75 ± 0.01 Å. This distance is slightly shorter than the Hg−Cl bond in $HgCl_2$ (1.78 Å),[86] which given the lower coordination number of this Hg species (0.82 ± 0.05 chlorines) suggests that Hg absorbs to a Cl^- ion in a monodentate inner-sphere complex rather than forming $HgCl_2$. The Hg−S pathway fit to the data resulted in a distance of 2.36 ± 0.01 Å, which is statistically the same as the Hg−S bond distance (2.367 Å) in cinnabar. This pathway is consistent with the μ-XANES data,

DOI: 10.1021/acs.energyfuels.5b01253
Energy Fuels 2015, 29, 6025−6038

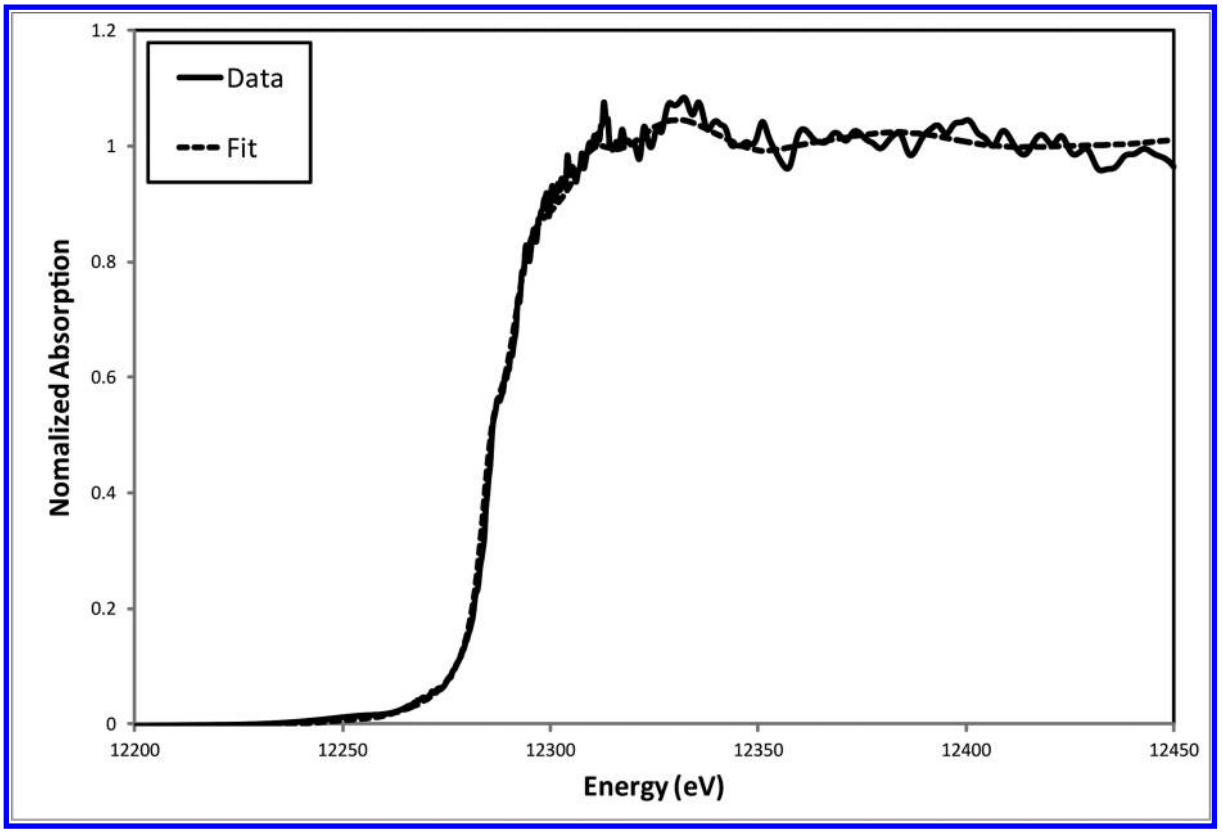

Figure 6. μ-XANES spectra and fit for the Hg hot spot seen in Figure 5B. The linear combination fit of the spectra is consistent with the presence of cinnabar (α-HgS).

which indicate that cinnabar is the dominant Hg-containing crystalline phase in the fly ash sample (Figure 6) and that metacinnabar, the metastable high-temperature polymorph of HgS with a conversion temperature of ~345 °C, is not detectable in the sample. The packed-bed reactor used in this study was operated at a temperature of ~140 °C, which is not sufficiently high to convert cinnabar to metacinnabar. The Hg−Br pathway at 2.77 ± 0.01 Å is consistent with the Hg−Br distance in the $Hg_3S_2Br_2$ model compound used in the fitting, which is similar to the mineral grechishchevite ($Hg_3S_2(Br,Cl)_2$), with a path distance of 2.75 Å.[87] Using $Hg_3S_2Br_2$ as a reference for the Hg−Br pathway is consistent with S in the 2− oxidation state, Hg in the 2+ oxidation state, and Br in the 1− oxidation state. Further support for this model for our samples comes from the fact that Br is highly correlated with Hg in the cinnabar-rich Hg hot spots as well as from the statistical validity of adding the additional Hg−Br pathway as indicated by Hamilton's *R*-factor ratio test.[84] Although interpretation of the Hg−Cl, Hg−S and Hg−Br pathways is fairly straightforward, interpretation of the Hg−O and Hg−Fe pathways is more complex as discussed next.

Two different Hg−O interatomic distances were fit to the EXAFS data. The shortest Hg−O pathway at 1.82 ± 0.01 Å is most likely the result of contributions from two different Hg−O bonds of similar interatomic distance. The shortest Hg−O bond is consistent with the 1.83 Å[53] distance of Hg^{2+} binding to a carboxylic acid functional group. This binding scheme is also supported by the shift to a higher energy of the 2848 and 2917 cm^{-1} FTIR absorption bands as well as a reduction in intensity of the carboxylic acid absorption peaks in the FTIR data following reaction (Figure 1B). Additionally, the Hg−O bond at 1.82 ± 0.01 Å is also consistent with Hg binding as a bidentate inner-sphere complex to iron oxide surfaces. This assertion is supported by the presence of an Hg−Fe scattering pathway at 3.09 ± 0.01 Å and the high spatial correlation between the Hg and Fe observed in the μ-XRF maps for the reacted fine ash (Figure 4). The distances for both the Hg−O and Hg−Fe pathways are shorter than those determined by Kim et al.,[44] which is expected since this earlier study found evidence for monodentate inner-sphere complexes of Hg(II) on goethite. In addition to the shorter distances of bidentate inner-sphere Hg(II) complexes versus those for monodentate Hg(II) complexes, the coordination numbers of the Hg−O and Hg−Fe species provide further evidence for a bidentate inner-sphere complex in our samples. The coordination number for the Hg−O species used in the fit is 1.74 ± 0.14 oxygens, whereas the coordination number for the Hg−Fe species is 0.84 ± 0.13 irons (Table 2). For a monodentate inner-sphere complex, the coordination numbers of both pathways should be similar, but in this instance the coordination number for the Hg−O pathway is more than twice that of the Hg−Fe pathway, suggesting a bidentate rather than a monodentate complex. Fitting of the EXAFS data for the shortest Hg−O interatomic distance in conjunction with XRF and FTIR data indicates that the shortest Hg−O interatomic distance is most likely the result of a combination of Hg bound to carboxylic acid functional groups and bidentate inner-sphere complexes of Hg(II) on iron oxide surfaces.

The longer Hg−O interatomic distance in the shell-by-shell fit at 2.65 ± 0.02 Å is most likely due to the single-scattering pathway of Hg to the double-bonded oxygen of the carboxylic acid functional group. Crystallographic studies of Hg bound to organic molecules indicate that the Hg−O interatomic distance

DOI: 10.1021/acs.energyfuels.5b01253
Energy Fuels 2015, 29, 6025−6038

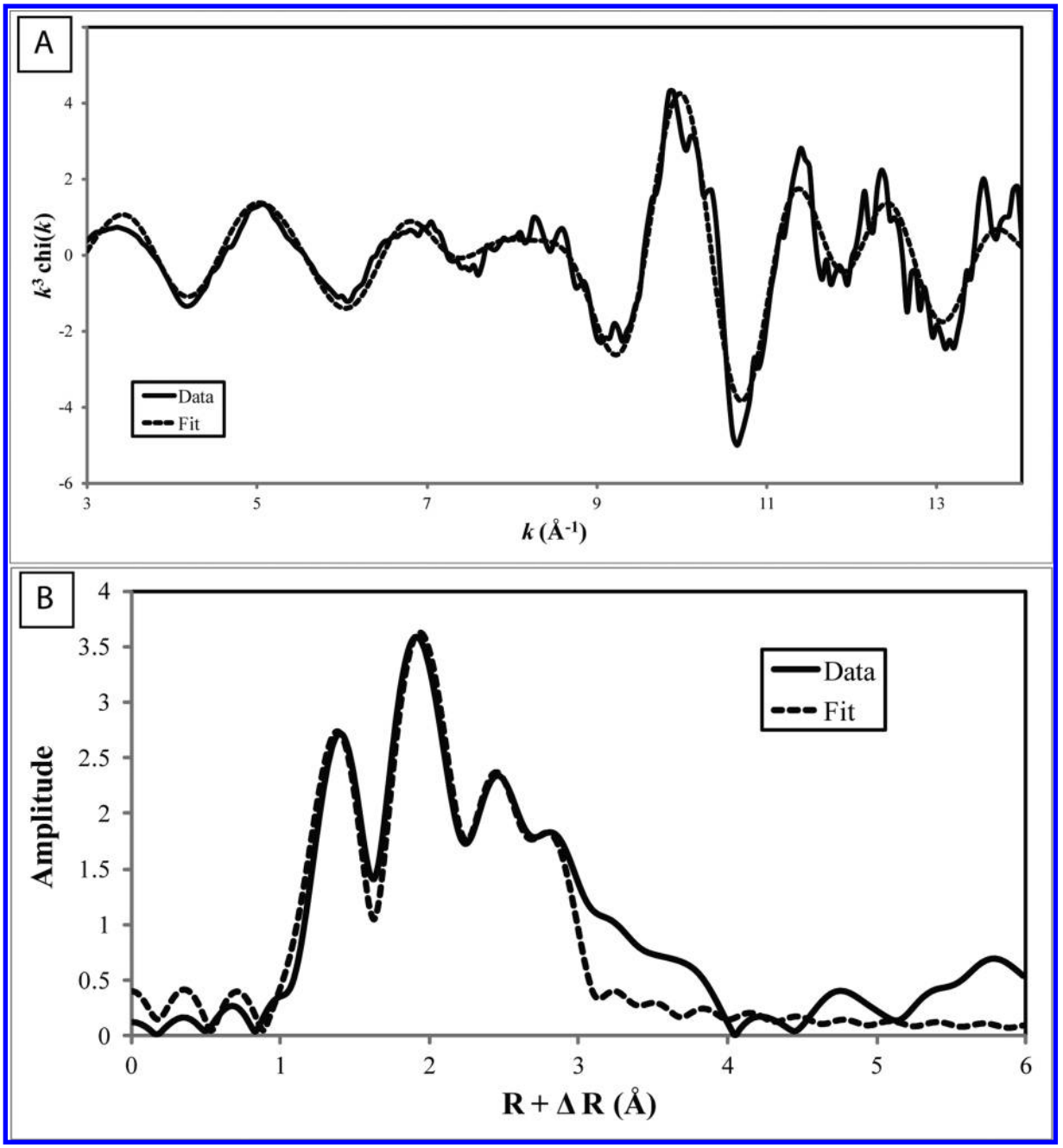

Figure 7. EXAFS spectra and Fourier transform for the reacted fine fly ash sample. (A) EXAFS spectra and shell-by-shell fit of data using six unique scattering pathways. Fitting parameters for each pathway are in Table 2. (B) Fourier transform and fit of the data for the reacted fine fly ash sample using six unique scattering pathways. Data from >3 Å in the Fourier transform are noise as indicated by the wavelet analysis of the spectra.

for the nonbinding, double-bonded oxygen in a carboxylic group is 2.66 ± 0.05 Å.[88,89] Thus, the distances for both Hg−O pathways in combination with the experimental and simulated FTIR data are indicative of Hg binding to carboxylic groups contained in the organic fraction of the fly ash. Though Hg may be binding to other types of organic functional groups in the fly ash, these complexes, if present, would constitute a minor fraction of the Hg−organic complexes when compared to the Hg−carboxylic acid complexes identified in the reacted fine ash.

Fitting of the EXAFS spectrum for the reacted ≤0.1 μm fraction using the shell-by-shell methods indicates a highly complex relationship between the fly ash and Hg. Though six Hg scattering pathways were fit to the data, interpretation of the pathways indicates that five types of Hg species dominate the spectrum: cinnabar, Hg−Br (either a sorption complex on cinnabar or a Hg−S−Br phase), Hg−Cl sorption complexes on iron oxides (hematite), Hg−iron oxide sorption complexes, and Hg−carboxylic acid sorption complexes on unburned organics. These different complexes have a wide range of Hg binding constants from as low as $10^{5.89}$ for acetic acid (analog for carboxylic acid functional groups) to as high as 10^{54} for cinnabar.[59] This wide range of binding constants makes it difficult to predict the stability of Hg in these samples, but the fits of the EXAFS data provide crucial insight into what phases of Hg are present in the fine fraction of coal power plant-derived fly ash.

DOI: 10.1021/acs.energyfuels.5b01253
Energy Fuels 2015, 29, 6025−6038

Table 2. Parameters Used in Fitting of EXAFS Spectra for the Reacted Fine Ash[a]

pathway	coordination no.	distance	σ^2
Hg−Cl	0.82 ± 0.05	1.75 ± 0.01	0.0040 ± 0.0003
Hg−O	1.74 ± 0.14	1.82 ± 0.01	0.0050 ± 0.0006
Hg−S	1.33 ± 0.10	2.36 ± 0.01	0.0045 ± 0.0005
Hg−O	0.64 ± 0.20	2.65 ± 0.02	0.0010 ± 0.0014
Hg−Br	1.49 ± 0.12	2.77 ± 0.01	0.0060 ± 0.0004
Hg−Fe	0.84 ± 0.13	3.09 ± 0.01	0.0048 ± 0.0008
E_0	−0.93 ± 0.83	reduced χ^2	16.48
S_0^2	0.9 ± 0.05	*R*-factor	0.0497

[a]Plots of the EXAFS fit and Fourier Transform are shown in Figure 7.

Table 3. Results of Hamilton's *R*-Factor Ratio Test for All Six Pathways Used in the EXAFS Fit[a]

path no.	*R*-factor ratio
1	N/A[b]
2	1.85
3	1.62
4	1.41
5	2.05
6	3.4

[a]When $b = 3$ and $n = 240$, the *R*-factor ratio for the 99.5% confidence level is 1.027. The order of the paths used in the fit start with path 1 being the shortest Hg−X scattering pathway distance, where X is an atom, and each additional pathway added is the next shortest scattering pathway distance. [b]N/A = not available.

CONCLUSIONS

A detailed study was carried out on the interaction of Hg vapor in a simulated flue gas stream with coal fly ash (bulk and ≤0.1 μm fractions). A variety of laboratory- and synchrotron-based mapping and spectroscopic techniques was used to determine (1) which size fraction dominates Hg uptake, (2) the elements with which Hg is associated, and (3) the Hg-containing species present in the fly ash samples. Elemental μ-XRF maps show that the ≤0.1 μm fraction is the dominant sink for Hg in the fly ash. The μ-XRF mapping also shows that Hg is associated with Fe and occurs as well in Fe-free hot spots, which represent Hg-containing or Hg-sorbed solid phases. μ-XRF mapping indicates that Fe is the only transition metal with which Hg is strongly positively correlated in our samples. Other transition metals as well as alkali and alkaline earth metals show no spatial correlation with Hg. The Hg hot spots are dominated by cinnabar and Hg correlated with Br, either as Hg−Br sorption complexes or a Hg−S−Br phase. Iron-associated Hg is dominated by bidentate inner-sphere complexes of Hg with iron oxides and Hg sorbed to chloride. Mercury was also found to bind to the carboxylic acid functional groups in the fly ash, but these organic regions are randomly scattered throughout the sample and are not associated with Fe or other metals.

The majority of the Hg phases found in coal fly ash reacted with the simulated coal power plant exhaust stream are more recalcitrant than would be the case if elemental Hg were physisorbed to the surface of the fly ash particles. The lack of detectable elemental Hg in the fly ash indicates that the volatilization potential of Hg from these samples is quite low and fairly stable with regard to ash being used for making additional consumer products. The results of this study suggest that the use of Hg-containing fly ash of the type examined in the present study in concretes, dry wall, and other consumer products should result in low Hg exposure.

AUTHOR INFORMATION

Corresponding Author

*E-mail: adamjew@stanford.edu.

Notes

The authors declare no competing financial interest.

ACKNOWLEDGMENTS

We thank Drs. Sam Webb, Benjamin Kocar, and John Bargar of the Stanford Synchrotron Radiation Lightsource for their assistance with data collection on beamlines 2-3 and 11-2. We also acknowledge the assistance of Mr. Robert Jones of the Stanford Nanocharacterization Laboratory in the use of the electron microprobe and SEM. Additional thanks go to Dr. Guangchao Li and Mr. Douglas Turner of the Stanford Environmental Measurements Laboratory for assistance with the FTIR and XRF data collection. We also acknowledge the high performance computing (HPC) facilities in the Center for Computational Earth and Environmental Science (CEES) at Stanford University. Funding for this work was made possible by the National Science Foundation (Grant No. 1235878) and the Stanford School of Earth Sciences (J.W. and G.E.B.). Support was also provided by NSF Cooperative Agreement EF-0830093 to the Center for the Environmental Implications of Nanotechnology (CEINT) (G.E.B.).

REFERENCES

(1) UNEP. *Global Mercury Assessment 2013: Sources, Emissions, Releases and Environmental Transport*; UNEP Chemicals Branch, United Nations Environmental Programme: Geneva, Switzerland, 2013; p 44.

(2) National Emission Standards for Hazardous Air Pollutants From Coal- and Oil-Fired Electric Utility Steam Generating Units and Standards of Performance for Fossil-Fuel-Fired Electric Utility, Industrial-Commercial-Institutional, and Small Industrial-Commercial-Institutional Steam Generating Units. *Federal Register*; United States Environmental Protection Agency: Washington, DC, USA, 2012; Vol. *77*, p 210.

(3) Chen, J.; Liu, G.; Kang, Y.; Wu, B.; Sun, R.; Zhou, C.; Wu, D. Atmospheric emissions of F, As, Se, Hg, and Sb from coal-fired power and heat generation in China. *Chemosphere* **2013**, *90*, 1925−1932.

(4) Goodarzi, F.; Huggins, F. E.; Sanei, H. Assessment of elements, speciation of As, Cr, Ni and emitted Hg for a Canadian power plan burning bituminous coal. *Int. J. Coal Geol.* **2008**, *74*, 1−12.

(5) Pacyna, E. G.; Pacyna, J. M. Global Emission of Mercury from Anthropogenic Sources in 1995. *Water, Air, Soil Pollut.* **2002**, *137*, 149−165.

(6) Pacyna, E. G.; Pacyna, J. M.; Sundseth, K.; Munthe, J.; Kindbom, K.; Wilson, S.; Steenhuisen, F.; Maxson, P. Global emission of mercury to the atmosphere from anthropogenic sources in 2005 and projections to 2020. *Atmos. Environ.* **2010**, *44*, 2487−2499.

(7) Pavageau, M.-P.; Pecheyran, C.; Krupp, E. M.; Morin, A.; Donard, O. F. X. Volatile Metal Species in Coal Combustion Flue Gas. *Environ. Sci. Technol.* **2002**, *36* (7), 1561−1573.

(8) Xu, M.; Qiao, Y.; Liu, J.; Zheng, C. Kinetic calculation and modeling of trace element reactions during combustion. *Powder Technol.* **2008**, *180*, 157−163.

(9) Yan, R.; Lu, X.; Zeng, H. Trace Elements in Chinese Coals and their Partitioning During Coal Combustion. *Combust. Sci. Technol.* **1999**, *145*, 57−81.

(10) Ozaki, M.; Uddin, M. A.; Sasaoka, E.; Wu, S. Temperature programmed decomposition desorption of the mercury species over spent iron-based sorbents for mercury removal from coal derived fuel gas. *Fuel* **2008**, *87*, 3610−3615.

DOI: 10.1021/acs.energyfuels.5b01253
Energy Fuels 2015, 29, 6025−6038

(11) Wu, S.; Oya, N.; Ozaki, M.; Kawakami, J.; Uddin, M. A.; Sasaoka, E. Development of iron oxide sorbents for Hg^0 removal from coal derived fuel gas: Sulfidation characteristics of iron oxide sorbents and activity for COS formation during Hg^0 removal. *Fuel* **2007**, *86*, 2857−2863.
(12) Wu, S.; Ozaki, M.; Uddin, M. A.; Sasaoka, E. Development of iron-based sorbents for Hg^0 removal from coal derived fuel gas: Effect of hydrogen chloride. *Fuel* **2008**, *87*, 467−474.
(13) Wu, S.; Uddin, M. A.; Sasaoka, E. Characteristics of the removal of mercury vapor in coal derived fuel gas over iron oxide sorbents. *Fuel* **2006**, *85*, 213−218.
(14) Shoji, T.; Huggins, F. E.; Huffman, G. P.; Linak, W. P.; Miller, C. A. XAFS Spectroscopy Analysis of Selected Elements in Fine Particulate Matter Derived from Coal Combustion. *Energy Fuels* **2002**, *16*, 325−329.
(15) Kouvo, P. Trace Metal Distribution and Control in the Pilot-Scale Bubbling Fluidized Bed Combustor Equipped with the Pulse-Jet Fabric Filter, Limestone Injection, and the Humidification Reactor. *J. Air Waste Manage. Assoc.* **2003**, *53*, 406−416.
(16) Lopez-Anton, M. A.; Diaz-Somoano, M.; Martinez-Tarazona, M. R. Retention of Elemental Mercury in Fly Ashes in Different Atmospheres. *Energy Fuels* **2007**, *21*, 99−103.
(17) Lopez-Anton, M. A.; Tascon, J. M. D.; Martinez-Tarazona, M. R. Retention of mercury in activated carbons in coal combustion and gasification flue gases. *Fuel Process. Technol.* **2002**, *77*−*78*, 353−358.
(18) Kostova, I. J.; Hower, J. C.; Mastalerz, M.; Vassilev, S. V. Mercury capture by selected Bulgarian fly ashes: Influence of coal rank and fly ash carbon pore structure on capture efficiency. *Appl. Geochem.* **2011**, *26*, 18−27.
(19) Jurng, J.; Lee, T. G.; Lee, G. W.; Lee, S.-J.; Kim, B. H.; Seier, J. Mercury Removal from Incineration Flue Gas by Organic and Inorganic Adsorbents. *Chemosphere* **2002**, *47*, 907−913.
(20) Huggins, F. E.; Huffman, G. P.; Linak, W. P.; Miller, C. A. Quantifying Hazardous Species in Particulate Matter Derived from Fossil-Fuel Combustion. *Environ. Sci. Technol.* **2004**, *38* (6), 1836−1842.
(21) Sasmaz, E.; Kirchofer, A.; Jew, A. D.; Saha, A.; Abram, D.; Jaramillo, T. F.; Wilcox, J. Mercury chemistry on brominated activated carbon. *Fuel* **2012**, *99*, 188−196.
(22) Wilcox, J.; Rupp, E.; Ying, S. C.; Lim, D.-H.; Negreira, A. S.; Kirchofer, A.; Feng, F.; Lee, K. Mercury adsorption and oxidation in coal combustion and gasification processes. *Int. J. Coal Geol.* **2012**, *90*−*91*, 4−20.
(23) Wilcox, J.; Sasmaz, E.; Kirchofer, A.; Lee, S. S. Heterogeneous Mercury Reaction Chemistry on Activated Carbon. *J. Air Waste Manage. Assoc.* **2011**, *61* (4), 418−426.
(24) Querol, X.; Alastuey, A.; Lopez-Soler, A.; Mantilla, E.; Plana, F. Mineral Composition of Atmospheric Particulates Around a Large Coal-Fired Power Station. *Atmos. Environ.* **1996**, *30* (21), 3557−3572.
(25) Kronbauer, M. A.; Izquierdo, M.; Dai, S.; Waanders, F. B.; Wagner, N. J.; Mastalerz, M.; Hower, J. C.; Oliveira, M. L. S.; Taffarel, S. R.; Bizani, D.; Silva, L. F. O. Geochemistry of ultra-fine and nano-compounds in coal gasification ashes: A synoptic view. *Sci. Total Environ.* **2013**, *456*−*457*, 95−103.
(26) Chen, Y.; Shah, N.; Huggins, F. E.; Huffman, G. P.; Linak, W. P.; Miller, C. A. Investigation of primary fine particulate matter from coal combustion by computer-controlled scanning electron microscopy. *Fuel Process. Technol.* **2004**, *85*, 743−761.
(27) Linak, W. P.; Yoo, J.-I.; Wasson, S. J.; Zhu, W.; Wendt, J. O. L.; Huggins, F. E.; Chen, Y.; Shah, N.; Huffman, G. P.; Gilmour, M. I. Ultrafine ash aerosols from coal combustion: Characterization and health effects. *Proc. Combust. Inst.* **2007**, *31*, 1929−1937.
(28) Chen, Y.; Shah, N.; Huggins, F. E.; Huffman, G. P. Transmission Electron Microscopy Investigation of Ultrafine Coal Fly Ash Particles. *Environ. Sci. Technol.* **2005**, *39* (4), 1144−1151.
(29) Huggins, F. E. Overview of analytical methods for inorganic constituents in coal. *Int. J. Coal Geol.* **2002**, *50*, 169−214.
(30) Vassilev, S. V.; Vassileva, C. G. Methods for Characterization of Composition of Fly Ashes frrom Coal-Fire Power Stations: A Critical Overview. *Energy Fuels* **2005**, *19*, 1084−1098.
(31) Goodarzi, F.; Huggins, F. E. Monitoring the species of arsenic, chromium and nickel in milled coal, bottom ash and fly ash from a pulverized coal-fired power plant in western Canada. *J. Environ. Monit.* **2001**, *3*, 1−6.
(32) Goodarzi, F.; Huggins, F. E. Speciation of Arsenic in Feed Coals and Their Ash Byproducts from Canadian Power Plants Burning Subbituminous and Bituminous Coals. *Energy Fuels* **2005**, *19*, 905−915.
(33) Huggins, F. E.; Huffman, G. P.; Kolker, A.; Mroczkowski, S. J.; Palmer, C. A.; Finkelman, R. B. Combined Application of XAFS Spectroscopy and Sequential Leaching for Determination of Arsenic Speciation in Coal. *Energy Fuels* **2002**, *16*, 1167−1172.
(34) Huggins, F. E.; Sanei, H. Synchrotron-radiation-induced oxidation of selenite to selenate in coal-derived fly ash. *J. Synchrotron Radiat.* **2011**, *18*, 530−533.
(35) Huggins, F. E.; Senior, C. L.; Chu, P.; Ladwig, K.; Huffman, G. P. Selenium and Arsenic Speciation in Fly Ash from Full-Scale Coal-Burning Utility Plants. *Environ. Sci. Technol.* **2007**, *41* (9), 3284−3289.
(36) Luo, Y.; Giammar, D. E.; Huhmann, B. L.; Catalano, J. G. Speciation of Selenium, Arsenic, and Zinc in Class C Fly Ash. *Energy Fuels* **2011**, *25*, 2980−2987.
(37) Collins, C. R.; Sherman, D. M.; Ragnarsdottir, K. V. Surface Complexation of Hg^{2+} on Goethite: Mechanism from EXAFS Spectroscopy and Density Functional Calculations. *J. Colloid Interface Sci.* **1999**, *219*, 345−350.
(38) Hutson, N. D.; Attwood, B. C.; Scheckel, K. G. XAS and XPS Characterization of Mercury Binding on Brominated Activated Carbon. *Environ. Sci. Technol.* **2007**, *41* (5), 1747−1752.
(39) Jew, A. D.; Kim, C. S.; Rytuba, J. J.; Gustin, M. S.; Brown, G. E., Jr. A New Technique for Quantification of Elemental Hg in Mine Wastes and Its Implications for Mercury Evasion Into the Atmosphere. *Environ. Sci. Technol.* **2011**, *45* (2), 412−417.
(40) Kim, C. S.; Bloom, N. S.; Rytuba, J. J.; Brown, G. E., Jr. Mercury Speciation by X-ray Absorption Fine Structure Spectroscopy and Sequential Chemical Extractions: A Comparison of Speciation Methods. *Environ. Sci. Technol.* **2003**, *37* (22), 5102−5108.
(41) Kim, C. S.; Brown, G. E., Jr.; Rytuba, J. J. Characterization and Speciation of Mercury-Bearing Mine Wastes Using X-ray Absorption Spectroscopy. *Sci. Total Environ.* **2000**, *261*, 157−168.
(42) Kim, C. S.; Rytuba, J. J.; Brown, G. E., Jr. EXAFS study of mercury(II) sorption to Fe- and Al-(hydr)oxides I: Effects of pH. *J. Colloid Interface Sci.* **2004**, *271*, 1−15.
(43) Kim, C. S.; Rytuba, J. J.; Brown, G. E., Jr. Geological and Anthropogenic Factors Influencing Mercury Speciation in Mine Wastes: An EXAFS Spectroscopy Study. *Appl. Geochem.* **2004**, *19*, 379−393.
(44) Kim, C. S.; Rytuba, J. J.; Brown, G. E., Jr. EXAFS study of mercury(II) sorption to Fe- and Al-(hydr)oxides II: Effects of chloride and sulfate. *J. Colloid Interface Sci.* **2004**, *270*, 9−20.
(45) Lowry, G. V.; Shaw, S.; Kim, C. S.; Rytuba, J. J.; Brown, G. E., Jr. Macroscopic and Microscopic Observations of Particle-Facilitated Mercury Transport from New Idria and Sulphur Bank Mercury Mine Tailings. *Environ. Sci. Technol.* **2004**, *38* (19), 5101−5111.
(46) Skyllberg, U.; Bloom, P. R.; Qian, J.; Lin, C.-M.; Bleam, W. F. Complexation of Mercury(II) in Soil Organic Matter: EXAFS Evidence for Linear Two-Coordination with Reduced Sulfur Groups. *Environ. Sci. Technol.* **2006**, *40* (13), 4174−4180.
(47) Skyllberg, U.; Qian, J.; Frech, W. Combined XANES and EXAFS Study on the Bonding of Methyl Mercury to Thiol Groups in Soil and Aquatic Organic Matter. *Phys. Scr.* **2005**, *T115*, 894−896.
(48) Slowey, A. J.; Rytuba, J. J.; Brown, G. E., Jr. Speciation of Mercury and Mode of Transport from Placer Gold Mine Tailings. *Environ. Sci. Technol.* **2005**, *39* (6), 1547−1554.
(49) Bernaus, A.; Gaona, X.; Ivask, A.; Kahru, A.; Valiente, M. Analysis of Sorption and Bioavailability of Different Species of Mercury on Model Soil Components Using XAS Techniques and Sensor Bacteria. *Anal. Bioanal. Chem.* **2005**, *382*, 1541−1548.

DOI: 10.1021/acs.energyfuels.5b01253
Energy Fuels 2015, 29, 6025−6038

(50) Bernaus, A.; Gaona, X.; van Ree, D.; Valiente, M. Determination of Mercury in Polluted Soils Surrounding a Chlor-Alkali Plant: Direct Speciation by X-ray Absorption Spectroscopy Techniques and Preliminary Geochemical Characterisation of the Area. *Anal. Chim. Acta* **2006**, *565*, 73−80.
(51) Lennie, A. R.; Charnock, J. M.; Pattrick, R. A. D. Structure of Mercury(II)-Sulfur Complexes by EXAFS Spectroscopic Measurements. *Chem. Geol.* **2003**, *199*, 199−207.
(52) Slowey, A. J.; Johnson, S. B.; Rytuba, J. J.; Brown, G. E., Jr. Role of Organic Acids in Promoting Colloidal Transport of Mercury from Mine Tailings. *Environ. Sci. Technol.* **2005**, *39* (20), 7869−7874.
(53) Oberdorster, G. Pulmonary Effects of Inhaled Ultrafine Particles. *Int. Arch. Occup. Environ. Health* **2000**, *74*, 1−8.
(54) Lieberman, R. N.; Teutsch, N.; Cohen, H. Chemical and Surface Transformations of Bituminous Coal Fly Ash Used in Israel Following Treatments with Acidic and Neutral Aqueous Solutions. *Energy Fuels* **2014**, *28*, 4657−4665.
(55) Liu, P.; Kendelewicz, T.; Brown, G. E., Jr.; Nelson, E. J.; Chambers, S. A. Reaction of water vapor with α-Al_2O_3(0001) and α-Fe_2O_3(0001) surfaces: synchrotron X-ray photoemission studies and thermodynamic calculations. *Surf. Sci.* **1998**, *417*, 53−65.
(56) Kendelewicz, T.; Kaya, S.; Newberg, J. T.; Bluhm, H.; Mulakaluri, N.; Moritz, W.; Scheffler, M.; Nilsson, A.; Pentcheva, R.; Brown, G. E., Jr. X-ray Photoemission and Density Functional Theory Study of the Interaction of Water Vapor with the Fe_3O_4(001) Surface at Near-Ambient Conditions. *J. Phys. Chem. C* **2013**, *117*, 2719−2733.
(57) Liu, P.; Kendelewicz, T.; Brown, G. E., Jr.; Parks, G. A.; Pianetta, P. Reaction of water with vacuum-cleaved CaO (100) surfaces: An X-ray photoemission spectroscopy study. *Surf. Sci.* **1998**, *416*, 326−340.
(58) Brown, G. E., Jr. Spectroscopic Studies of Chemisorption Reaction Mechanisms at Oxide-Water Interfaces. *Rev. Mineral.* **1990**, *23*, 309−364.
(59) Smith, R. M.; Martell, A. E., *NIST Critically Selected Stability Constants of Metal Complexes Database: Version 8.0*, NIST Standard Reference Database 46; National Institute of Standards and Technology: Washington, DC, USA, 2004.
(60) Rupp, E. C.; Wilcox, J. Mercury chemistry of brominated activated carbons-Packed-bed breakthrough experiments. *Fuel* **2014**, *117*, 351−353.
(61) Korpiel, J. A.; Vidic, R. D. Effect of Sulfur Impregnation Method of Activated Carbon Uptake of Gas-Phase Mercury. *Environ. Sci. Technol.* **1997**, *31* (8), 2319−2325.
(62) *Jade XRD Pattern Processing*, Ver. 6.5; Materials Data: Livermore, CA, USa, 2002.
(63) Lande, J.; Webb, S. M. *The Area Diffraction Machine Program*; Stanford Synchrotron Radiation Laboratory: Menlo Park, CA, USA, 2007.
(64) *Method 1631, Revision E: Mercury in Water by Oxidation, Purge and Trap, and Cold Vapor Atomic Fluorescence Spectrometry*.United States Environmental Protection Agency: Washington, DC, USA, 2002.
(65) Birk, J. P. *Chemistry*; Houghton Mifflin: Boston, MA, 1994; p 1035.
(66) Wade, L. G., Jr. *Organic Chemistry*, 5th ed.; Prentice Hall: Upper Saddle River, NJ, USA, 2003; p 1220.
(67) Petrucci, R. H.; Harwood, W. S.; Herring, F. G.; Madura, J. D. *General Chemistry: Principles & Modern Applications*. 9th ed.; Prentice Hall: Upper Saddle River, NJ, USA, 2007; p 1172.
(68) Silberberg, M. S. *Chemistry: The Molecular Nature of Matter and Change*, 2nd ed.; McGraw-Hill: Boston, MA, USA, 2000; p 1086.
(69) Salisbury, J. W.; Walter, L. S.; Vergo, N.; D'Aria, D. M. *Infrared (2.1−25 μm) Spectra of Minerals*. The Johns Hopkins University Press: Baltimore, MD, USA, 1991; p 267.
(70) Clark, S. J.; Segall, M. D.; Pickard, C. J.; Hasnip, P. J.; Probert, M. I. J.; Refson, K.; Payne, M. C. First Principles Methods using CASTEP. *Z. Kristallogr.* **2005**, *220*, 567−570.
(71) Hohenberg, P.; Kohn, W. Inhomogeneous electron gas. *Phys. Rev.* **1964**, *136*, 864−871.
(72) Kohn, W.; Sham, L. J. Self-consistent equations including exchange and correlation effects. *Phys. Rev.* **1965**, *140*, A1133−A1138.
(73) Payne, M. C.; Teter, M. P.; Allan, D. C.; Arias, T. A.; Joannopoulos, J. D. Iterative Minimization for ab Initio Total-Energy Calculations: Molecular Dynamics and Conjugate Gradients. *Rev. Mod. Phys.* **1992**, *64*, 1045−1097.
(74) *Opium-pseudopotential generation project*, Sourceforge.net, 2009.
(75) Lee, M. H. Doctoral Thesis, Cambridge University, 1996.
(76) Perdew, J. P.; Burke, K.; Ernzerhof. Generalized gradient approximation made simple. *Phys. Rev. Lett.* **1996**, *77*, 3865−3868.
(77) Pfrommer, B. G.; Cote, M.; Louie, S.; Cohen, M. L. Relaxation of Crystals with the Quasi-Newton Method. *J. Comput. Phys.* **1997**, *131*, 233−240.
(78) Accelrys, I. *Materials Studio*, Ver. 6.0; Biovia: San Diego, CA, USA, 2012.
(79) Refson, K.; Tulip, P. R.; Clark, S. J. Variational density-functional perturbation theory for dielectrics and lattice dynamics. *Phys. Rev. B: Condens. Matter Mater. Phys.* **2006**, *73*, 155114.
(80) Webb, S. *SMAK: Sam's Microprobe Analysis Kit*, Ver. 0.50; Stanford Synchrotron Radiation Laboratory: Menlo Park, CA, USA, 2006.
(81) Webb, S. *SixPACK*, 0.63; Stanford Synchrotron Radiation Laboratory: Menlo Park, CA, USA, 2006.
(82) Webb, S. M. SIXPack: a graphical user interface for XAS analysis using IFEFFIT. *Phys. Scr.* **2005**, *T115*, 1011−1014.
(83) Ankudinov, A. L.; Ravel, B.; Rehr, J. J.; Conradson, S. D. Real-space Multiple-scattering Calculation and Interpretation of X-ray Absorption Near-edge Structure. *Phys. Rev. B: Condens. Matter Mater. Phys.* **1998**, *58* (12), 7565−7576.
(84) Hamilton, W. C. Significance Tests on the Crystallographic R Factor. *Acta Crystallogr.* **1965**, *18*, 502−510.
(85) Munoz, M.; Argoul, P.; Farges, F. Continuous Cauchy wavelet transform analyses of EXAFS spectra: A qualitative approach. *Am. Mineral.* **2003**, *88*, 694−700.
(86) Nieuwenkamp, W.; Bijvoet, J. Die Kristallstruktur von Bleibromid $PbBr_2$. *Z. Kristallogr. - Cryst. Mater.* **1933**, *84*, 49−61.
(87) Voroshilov, Y. V.; Khudolij, V. A.; Pan'ko, V. V.; Minets, Yh. V. Phase equilibria in HgS-HgTe-$HgBr_2$ system and crystal structure of $Hg_3S_2Br_2$ and Hg_3TeBr_4 Compounds. *Inorg. Mater.* **1996**, *32* (12), 1281−1286, http://serials.unibo.it/cgi-ser/start/en/spogli/df-s.tcl?prog_art=41804&language=ENGLISH&view=articoli.
(88) Halfpenny, J.; Small, R. W. H. Structure of Tris(pyridine) mercury(II)Bis(trifluoroacetate). *Acta Crystallogr., Sect. B: Struct. Crystallogr. Cryst. Chem.* **1978**, *B34*, 3758−3760.
(89) Halfpenny, J.; Small, R. W. H. The Structure of Phenyl(pyridine)-mercury(II) Trifluoroacetate. *Acta Crystallogr., Sect. B: Struct. Crystallogr. Cryst. Chem.* **1980**, *B36*, 938−940.

DOI: 10.1021/acs.energyfuels.5b01253
Energy Fuels 2015, 29, 6025−6038